





RESEARCH ARTICLE | MAY 10 2022

## Dynamic characteristics of droplet impact on vibrating superhydrophobic substrate

Chensen Lin (林晨森) ; Shuo Chen (陈硕) ; Ping Wei (韦萍) ; Lanlan Xiao (肖兰兰); Dongxiao Zhao (赵东晓) ; Yang Liu (刘扬)



*Physics of Fluids* 34, 052005 (2022)

<https://doi.org/10.1063/5.0090184>



View  
Online



Export  
Citation

### Articles You May Be Interested In

Dynamics of droplet impact on a ring surface

*Physics of Fluids* (January 2022)

A new surface design for molecular combing: A dissipative particle dynamics study

*J. Appl. Phys.* (September 2022)

Retraction and bouncing dynamics of nanodroplets upon impact on superhydrophobic surfaces

*Physics of Fluids* (March 2023)



Physics of Fluids

Special Topics Open  
for Submissions

[Learn More](#)

# Dynamic characteristics of droplet impact on vibrating superhydrophobic substrate

Cite as: Phys. Fluids **34**, 052005 (2022); doi: [10.1063/5.0090184](https://doi.org/10.1063/5.0090184)

Submitted: 3 March 2022 · Accepted: 21 April 2022 ·

Published Online: 10 May 2022



Chensen Lin (林晨森),<sup>1,2</sup> Shuo Chen (陈硕),<sup>1,2,a)</sup> Ping Wei (韦萍),<sup>1,2</sup> Lanlan Xiao (肖兰兰),<sup>3</sup> Dongxiao Zhao (赵东晓),<sup>4</sup> and Yang Liu (刘扬)<sup>5</sup>

## AFFILIATIONS

<sup>1</sup>School of Aerospace Engineering and Applied Mechanics, Tongji University, Shanghai 200092, China

<sup>2</sup>Shanghai Key Lab of Vehicle Aerodynamics and Vehicle Thermal Management Systems, Tongji University, Shanghai 201804, China

<sup>3</sup>School of Mechanical and Automotive Engineering, Shanghai University of Engineering Science, Shanghai 201620, China

<sup>4</sup>UM-SJTU Joint Institute, Shanghai Jiao Tong University, Shanghai 200240, China

<sup>5</sup>Department of Mechanical Engineering, The Hong Kong Polytechnic University, Hong Kong, China

<sup>a)</sup> Author to whom correspondence should be addressed: [schen\\_tju@tongji.edu.cn](mailto:schen_tju@tongji.edu.cn)

## ABSTRACT

The vibration of solids is ubiquitous in nature and in industrial applications and gives rise to alternative droplet dynamics during impact. Using many-body dissipative particle dynamics, we investigate the impact of droplets on superhydrophobic solid surfaces vibrating in the vertical direction at a vibration period similar to the contact time. Specifically, we study the influence of the impact phase and vibration frequency. We evaluate the influence from the aspects of maximum spreading diameter, the solid–liquid contact time and area, and the momentum variation during the impact. To quantitatively evaluate the solid–liquid contact, we introduce the area-time integral, which is the integral of the contact area over the whole contact time. It is meaningful when the heat exchange between solid and liquid is considered. One characteristic phenomenon of droplets impacting vibrating substrate is that multiple contacts may occur before the final rebound. Unlike previous studies defining the contact time as the time span from the first impact to the final detachment, we define the contact time as the summation of each individual contact time. Using this definition, we show that the discontinuity at the critical impact phase disappears. The fact that the area-time integral also changes continually with the impact phase supports the assumption that the effect of impact phase on the solid–liquid contact may be continuous. Moreover, we show that the probability of impact phase is affected by the vibrating frequency and use it to calculate the weighted averaged outcome when the impact phase is not controlled. This study not only offers insights into the physics of droplet impact on vibrating surfaces but also can be used to guide the design of surfaces to achieve manageable wetting using vibration.

Published under an exclusive license by AIP Publishing. <https://doi.org/10.1063/5.0090184>

## I. INTRODUCTION

Droplets impacting solid surfaces is a key element of a wide variety of phenomena encountered in both nature<sup>1,2</sup> and industry.<sup>3–5</sup> Different outcomes, such as bounce off, splash, or fully/partially deposited on the surface, depend on many factors, such as impact velocity, droplet size, surface morphology, and wettability. In applications such as anti-dew/icing<sup>6</sup> and anti-corrosion,<sup>7</sup> droplet rebound is favorable, and contact between liquid and solid should be reduced. On the contrary, in spray cooling,<sup>8</sup> ink-jet printing,<sup>9</sup> and other applications involving droplet deposition, contact between liquid and solid should be maximized.

Many studies have been conducted on droplet impact on stationary solid substrates. One of the essential outcomes of droplets impacting a

solid is the maximum spreading diameter. This quantity, pertinent in the absence of splash, has applications in ink-jet printing<sup>10</sup> and forensic science.<sup>11</sup> Numerous relations between the maximum spreading diameter and the impact parameters have been established based on the balance between inertia and viscous and capillary contributions.<sup>12,13</sup> Another essential factor is the contact time. Richard *et al.*<sup>14</sup> demonstrated that the contact time of a droplet impacting a smooth hydrophobic surface is almost constant, independent of the impact velocity, but grows linearly with droplet size. More aspects of droplet impact stationary substrate can be found in the review papers.<sup>12,15,16</sup>

On the other hand, vibrating is ubiquitous. Many surfaces are not stationary and oscillate at frequencies ranging from a few Hz to hundreds of Hz, for example, flying insect wings,<sup>17</sup> turbine blades,<sup>18</sup>

pumps and compressors,<sup>19</sup> and automotive systems.<sup>20</sup> These solids vibrate either actively or passively. For active vibrating, people have realized that vibration can help us to enhance condensation,<sup>21</sup> control droplet spreading,<sup>22</sup> or promote the droplet to transient from Wenzel state to Cassie–Baxter state on textured surfaces.<sup>23–25</sup> For passive vibrating in applications like aircraft, it is vitally important to consider vibration in droplet impact research because it is related to safety. However, only a handful of studies have characterized the physics of droplet impact in the presence of solid vibration.

Weisensee *et al.*<sup>26</sup> investigated the dynamics of droplet impact by conducting experiments on vibrating rigid and elastic superhydrophobic surfaces. They reported a variation of 60%–160% in terms of contact time compared to the stationary surfaces. Moreover, a discontinuity of contact time is observed at a specific impact phase. We comment here that the definition of contact time accounts for this discontinuity, and we will discuss it in detail in our paper. They also stated that the most influential factor on impact dynamics is the phase difference between the droplet and solid motions, while amplitude does not directly change the impact outcomes. Moradi *et al.*<sup>27</sup> numerically investigated the impact of droplets on low-adhesion solid surfaces vibrating in the vertical direction. According to their findings, surface wettability also affects the outcomes. As the surface contact angle is reduced, surface vibration exhibits a more substantial influence, and the dependency of the contact time and droplet rebound velocity on the phase angle become more apparent. Lee and Kim<sup>28</sup> conducted experiments on the recoiling dynamics of droplets upon impact vibrating solids and found that upward motion of the solid at the moment of impact promotes droplet rebound, while downward motion suppresses the rebound.

One motivation of our work is that the contact area was usually neglected in previous studies. The contact area is essential as well as the contact time if heat exchange is involved. The spreading lamella along the substrate can dramatically increase the contact area, thus increasing the contact. Girard *et al.*<sup>29</sup> pointed out the problem and used the integral of contact area over time to determine the contact on a stationary patterned substrate. Inspired by Girard *et al.*, in this paper, we first apply the concept of area-time integral on the vibration surface to inspect the influence of vibration from a new perspective.

Another motivation of our work is the reported phenomenon of contact time's discontinuity at the critical impact phase, which has been reported for relatively high frequencies.<sup>26</sup> Since area-time integral characterizes the solid–liquid contact as well as contact time but from a different perspective, we hope to further explore the cause of the discontinuity and make the conclusion consistent with the area-time integral results.

In addition to the experimental research, various numerical models have been applied to approach the droplet impact problem, for example, computational fluid mechanics,<sup>13</sup> lattice Boltzmann methods,<sup>27,30</sup> and dissipative particle dynamics (DPD).<sup>31</sup> DPD<sup>32,33</sup> is a mesoscale particle-based method, and it has been widely used in problems like red blood cells,<sup>34–37</sup> droplets or bubbles,<sup>38–42</sup> colloids,<sup>43</sup> and polymer.<sup>44,45</sup> There is also some pioneering work integrating machine learning techniques with the DPD simulations.<sup>46</sup>

DPD is a relatively mature research tool for droplet impacting problems. The simulation results have been compared with the experimental footage from a morphological perspective and showed good agreement.<sup>31</sup> The transient impacting force on the solid is also

measured and validated with experimental data.<sup>47</sup> The results showed that the dimensionless DPD temporal evolution of impact force agrees well with the dimensionless equation,<sup>48</sup> which captures the similarity of experimental data covering a wide range of *We* and *Re*. Compared to the experimental method, DPD has many advantages. For example, the contact area can be easily measured by counting the particles within a cutoff range of solid, while, in the experiment, it can only be inferred indirectly with many difficulties, such as limitation of view and the distortion from the liquid. Therefore, DPD has been applied in many related research, including droplet impacting stationary solid cylinder,<sup>49,50</sup> solid sphere,<sup>51</sup> ring decorated substrate,<sup>51</sup> crater-like substrate,<sup>47</sup> etc.

This paper focuses on the droplet impact on vibrating hydrophobic substrates. The aim is to investigate the effects of impact phase and vibration frequency on the dynamics of droplets, including the maximum spreading diameter, the solid–liquid contact time and area, and the momentum variation during the impact. First, we introduce the DPD method and the setup in Sec. II. Then, we discuss the computational results in Sec. III. Finally, we end the paper with a summary in Sec. IV.

## II. METHODS AND MODEL CONFIGURATIONS

### A. Methods

Our model is built on the framework of dissipative particle dynamics (DPD). As a discrete particle methods, DPD inherits the same algorithm as a molecular dynamics system, which is based on Newton's second law:

$$m_i \frac{d^2 \mathbf{r}_i}{dt^2} = m_i \frac{d\mathbf{v}_i}{dt} = \mathbf{F}_i = \sum_{j \neq i} (\mathbf{F}_{ij}^C + \mathbf{F}_{ij}^D + \mathbf{F}_{ij}^R), \quad (1)$$

where  $m_i$ ,  $\mathbf{r}_i$ ,  $\mathbf{v}_i$ , and  $\mathbf{F}_i$  denote mass, position vector, velocity vector, and force vector, respectively, of particle with index  $i$ . The calculation of  $\mathbf{F}_i$  is carried out over all neighboring particles within a cutoff range. Beyond the cutoff range, all interactions are neglected. The pairwise force contains three parts: the conservative force  $\mathbf{F}_{ij}^C$ , the dissipative force  $\mathbf{F}_{ij}^D$ , and the random force  $\mathbf{F}_{ij}^R$ , which can be written as

$$\begin{aligned} \mathbf{F}_{ij}^C &= a_{ij} \omega^C(r_{ij}) \mathbf{e}_{ij}, \\ \mathbf{F}_{ij}^D &= -\gamma_{ij} \omega^D(r_{ij}) (\mathbf{v}_i - \mathbf{v}_j) \mathbf{e}_{ij}, \\ \mathbf{F}_{ij}^R &= \sigma_{ij} \omega^R(r_{ij}) \theta_{ij} \delta t^{-1/2} \mathbf{e}_{ij}, \end{aligned} \quad (2)$$

where the coefficients  $a_{ij}$ ,  $\gamma_{ij}$ , and  $\sigma_{ij}$  reflect the strength of conservative, dissipative, and random force, respectively. Here,  $r_{ij} = |\mathbf{r}_i - \mathbf{r}_j|$  is the distance between two neighboring particles  $i$  and  $j$ ,  $\mathbf{e}_{ij} = \mathbf{r}_{ij}/r_{ij}$  is the unit vector,  $\mathbf{v}_{ij} = \mathbf{v}_i - \mathbf{v}_j$  is the difference of their velocities, and  $\theta$  is a Gaussian white noise ( $\theta_{ij} = \theta_{ji}$ ). To satisfy the fluctuation-dissipation theorem (FDT),<sup>52</sup> two conditions must be enforced:  $\sigma_{ij}^2 = 2\gamma_{ij}k_B T$  and  $\omega^D(r_{ij}) = [\omega^R(r_{ij})]^2$ .

Because the equation of state of DPD does not contain a van der Waals loop, the standard DPD formalism excludes the possibility of simulating phenomena involving free surface or vapor–liquid coexistence. To this end, Warren<sup>53</sup> modified the conservative force term to include both attractive and repulsive components and established the many-body dissipative particle method (MDPD). The conservative force of MDPD depends not only on the inter-particle distance but also on the instantaneous local particle density,

$$\mathbf{F}_{ij}^C = A_{ij}w_c(r_{ij})\mathbf{e}_{ij} + B_{ij}(\rho_i + \rho_j)w_d(r_{ij})\mathbf{e}_{ij}. \quad (3)$$

The repulsive contribution in Eq. (3) is set to act within a shorter range  $r_d < r_c$  than the soft pair attractive potential to maintain a stable interface. The many-body repulsion is chosen in the form of a self-energy per particle, which is quadratic in the local density,  $B_{ij}(\rho_i + \rho_j)w_d(r_{ij})$ , where  $B > 0$ . The density of each particle is defined as  $\bar{\rho}_i = \sum_{j \neq i} w_\rho(r_{ij})$ , and its weight function  $w_\rho$  is defined as  $w_\rho = \frac{15}{2\pi r_d^3} (1 - \frac{r}{r_d})^2$ , where  $w_\rho$  vanishes for  $r > r_d$ .

## B. Modeling of droplets and vibrating substrates

We construct a system consisting of a liquid droplet and a vibrating solid substrate, see Fig. 1(a). The simulation box has dimensions  $\{L_x, L_y, L_z\} = \{200, 200, 200\}$ , with periodic boundary conditions imposed on the  $x$  and  $y$  boundaries. Figure 1(b) is the diagram of the setup. The solid plate is comprised of frozen thermal equilibrium MDPD particles, and it can be treated as smooth macroscopically.<sup>54</sup> Throughout the paper, the droplet radius is denoted by  $R$ , and the impacting speed is denoted by  $U_0$ .

Figure 1(c) shows the position of the solid substrate as a function of time. The solid is vibrating around  $z = 0$  following a sinusoidal signal. The magnitude is denoted by  $a$ , and the vibration period of solid is denoted by  $T_s$ . We denote the phase angle of solid when the droplet impacts the substrate by  $\phi$ , which is presented in degrees in this study.

The DPD potential parameters used in this study are the same as in Lin *et al.*,<sup>31</sup> which have been validated with experimental data in droplet impacting problems. The parameters are as follows:  $A_{ll} = -80$ ,  $B_{ll} = 20$ ,  $A_{ls} = -5$ ,  $B_{ls} = 20$ ,  $r_c = 1.0$ ,  $r_d = 0.75$ ,  $\gamma_{ll} = 0.5$ , and  $\gamma_{ls} = 0.5$ . The subscript  $ll$  means liquid–liquid interaction, and  $ls$  means solid–liquid interaction.  $A$  and  $B$  are parameters in Eq. (3), and they control the attractive and repulsive force between MDPD particles, respectively.  $r_c$  and  $r_d$  are cutoff range of attractive and repulsive force in Eq. (3), respectively.  $\gamma$  controls the MDPD fluid viscosity. These values are widely used parameters for MDPD liquid/vapor systems, and more details on choosing the parameters can be found in Arienti *et al.*<sup>32</sup>

The measured liquid properties are as follows in DPD units: density  $\rho = 10.91$ , dynamic viscosity  $\mu = 27.25$ , surface tension  $\sigma = 49.82$ , and contact angle  $CA \approx 155^\circ$ . The droplet contains 753571 DPD particles with radius  $R = 25.0$ . The default impact velocity  $U_0 = 2.8$ , which leads to  $We = \rho U_0^2 D / \sigma = 85.8$ . Other

dimensionless numbers are  $Re = \rho U_0 D / \mu = 56.1$ ,  $Ca = \mu U_0 / \sigma = 1.53$ , and  $Oh = \mu / \sqrt{\rho \sigma D} = 0.16$ . To ensure the no-slip boundary condition and no penetration of liquid particles into the solid structure, we adopt the boundary condition method for arbitrary complex geometries proposed by Li *et al.*<sup>55</sup>

To better evaluate the behaviors of droplets, in addition to the maximum spreading diameter and contact time, we focus on the area-time integral during the impacting process. The area-time integral,  $I$ , is the integral of the liquid–solid contact area over time,<sup>29</sup>

$$I = \int_0^{T_c} A_c(t) dt, \quad (4)$$

where  $A_c(t)$  is the contact area at time  $t$  and  $T_c$  is the overall contact time. It is used to quantitatively evaluate the influence on the contact time and contact area. We set the  $I$  with a stationary plane surface as the reference  $I_0$ . Then, we could easily learn the effect of a vibrating surface by comparing  $I$  with  $I_0$ . The  $A_c(t)$  is measured by counting the liquid particles within the unit length range of solid particles and dividing it by the liquid density.

Droplets impacting a non-vibrating solid surface displayed the traditional spreading, recoil, and liftoff. The contact time has been proven to be irrelevant of the impacting speed.<sup>14</sup> For DPD droplets with an initial diameter  $D_0 = 50$ , the contact time  $T_c = 112.0$ . We use it as a reference time,  $T_{c,ref}$ , to evaluate the influence of vibration. Since the rebound of droplet can be understood as an oscillation (the droplet is a spring of stiffness  $\sigma$  and mass of  $\rho D_0^3$ , which oscillates with a constant period  $\sqrt{\rho D_0^3 / \sigma}$ ), the reference contact time also reflects the eigenfrequency of the droplet.<sup>56</sup>

In this study,  $T_{c,ref}$  is also used to determine the dimensionless vibrational frequency,  $f \equiv T_{c,ref} / T_s$ . We set default  $\hat{f} = 1.0$  in this study unless stated otherwise. The impacting speed  $U_0 = -2.8$  is constant throughout the paper, which is 2 times of the maximum solid speed when  $\hat{f} = 1.0$ .

All properties in the DPD model are in DPD units, which are non-dimensional. Once the target liquid properties are determined, the scaling relationships can be established. For example, to map the above-mentioned MDPD liquid properties ( $\rho$ ,  $\mu$ , and  $\sigma$ ) to liquid water at room temperature, the explicit DPD units are as follows:  $[l_{DPD}] = 5.56 \times 10^{-5}$  m,  $[t_{DPD}] = 1.04 \times 10^{-4}$  s, and  $[m_{DPD}] = 1.57 \times 10^{-11}$  kg. Any values in non-dimensional DPD units can be converted to physical properties using these relationships and vice versa.

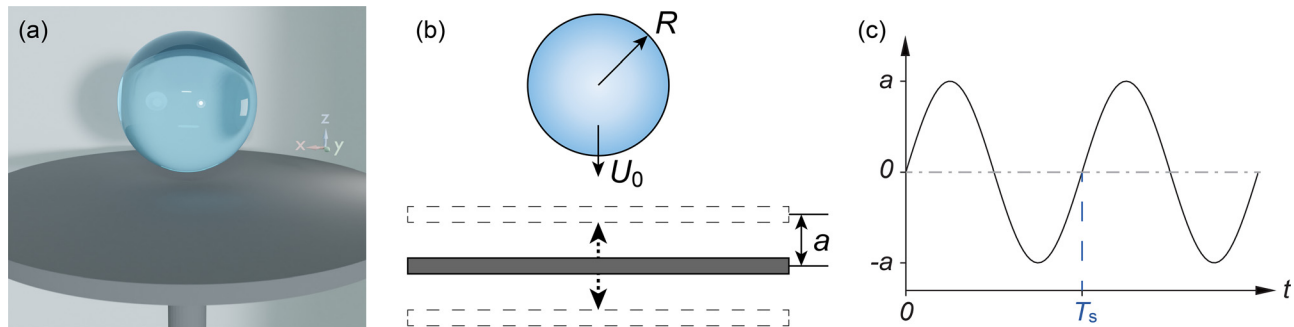


**FIG. 1.** (a) The 3-D view of the initial state of a spherical droplet to impact a vibrating solid surface. (b) The schematic diagram of the model setup. (c) The trajectory of the solid substrate as a function of time.

To map to another liquid, like silicon oil, the scaling relationships should be derived again, and they will all be different. For generality, we show simulation results in DPD units in Secs. III and IV as most previous DPD works do.

Before showing results on vibrating solids, we conducted a simple comparison of our MDPD model and experimental results. The comparison is for droplets impacting stationary flat surfaces, where plenty of experimental observations exist. Figure 2(a) shows the contact time,  $T$ , as a function of  $We$ . The contact time has been studied and shown to scale as  $\sqrt{\rho D_0^3 / \sigma}$  and is independent of the impact velocity  $U_0$ .<sup>14,57</sup> The measured  $T$  of simulation is also invariant with  $U_0$ , showing good agreement with the experimental observation. Figure 2(b) shows the maximum spreading diameter,  $D_{\max}$ , as a function of  $We$ . The dashed line indicates the slope 1/4, which is the law obtained by fitting experimental data.<sup>57</sup> Our MDPD results generally follow the trend but start to deviate as the spreading is close to splashing, where the  $D_{\max}$  becomes difficult to determine and measure. The results show that our model captures the dynamic characteristics of droplet well.

### III. RESULTS AND DISCUSSION

#### A. The effect of impacting phase

From previous studies,<sup>26,27</sup> we know the impact phase is the most important factor affecting droplet dynamics. In this section, we

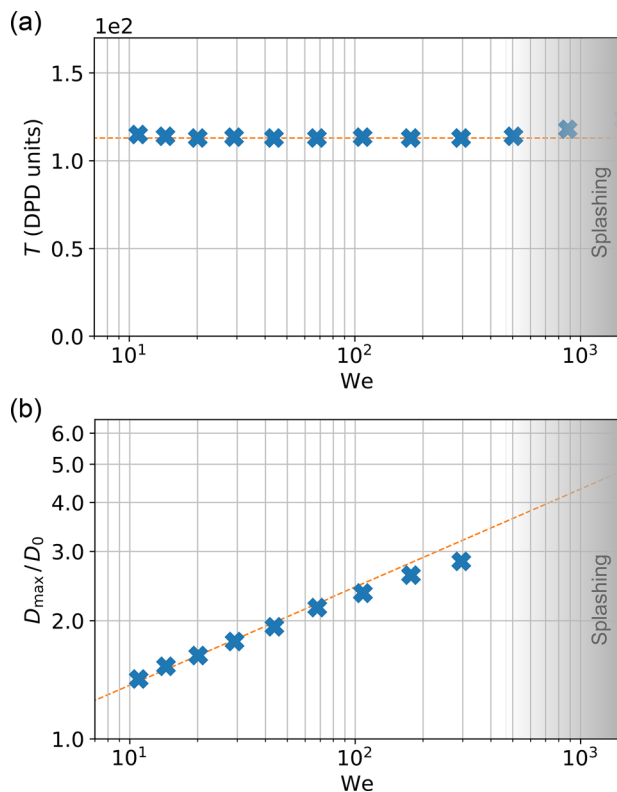


**FIG. 2.** Validation of our model for droplet impacting stationary solid surface. (a) The contact time as a function of  $We$ . The contact time should be independent of the impact velocity (dashed line). (b) The maximum spreading diameter,  $D_{\max}$ , as a function of  $We$ . The dashed line indicates the slope 1/4, which is the law obtained by fitting experimental data.

evaluate the influence of the impact phase from many aspects, including the maximum diameter, the momentum variation, the contact time, and the area-time integral.

Figure 3 is the snapshots of the droplets impacting the solid at different phases. The impact phase ( $\phi$ ) is presented in degrees.  $\phi = 90^\circ$  [Fig. 3(b)] and  $\phi = 270^\circ$  [Fig. 3(d)] denote that the impact happens when the solid plate is at its highest and lowest point;  $\phi = 0^\circ$  [Fig. 3(a)] and  $\phi = 180^\circ$  [Fig. 3(c)] denote that the impact happens when the solid plate is moving through the equilibrium position ( $z = 0$ ) at maximum speed upward and downward.

The snapshots show how the impacting phase affects the droplet's shape evolution. For  $\phi = 0^\circ$ , the droplets spread more expansive than the other cases and detach from the solid before the droplet recoils. On the contrary, the  $\phi = 180^\circ$  case shows the smallest spreading diameter. Due to the interplay of surface tension and the movement of solid, many shapes emerge, which have not been observed in traditional impact problems, such as the conical chocolate shape ( $\phi = 90^\circ$ ,  $t_{\text{DPD}} = 72$ ) and the mushroom shape ( $\phi = 270^\circ$ ,  $t_{\text{DPD}} = 60$ ). Furthermore, the contact time varies with  $\phi$  when the impact speed is the same. In addition, the detach shape is also strongly dependent on  $\phi$ . For  $\phi = 0^\circ$ , the droplet detaches from the solid substrate as it is widely spread ( $t_{\text{DPD}} = 39$ ). For  $\phi = 180^\circ$ , the droplet detaches from the solid as it is vertically elongated ( $t_{\text{DPD}} = 108$ ).

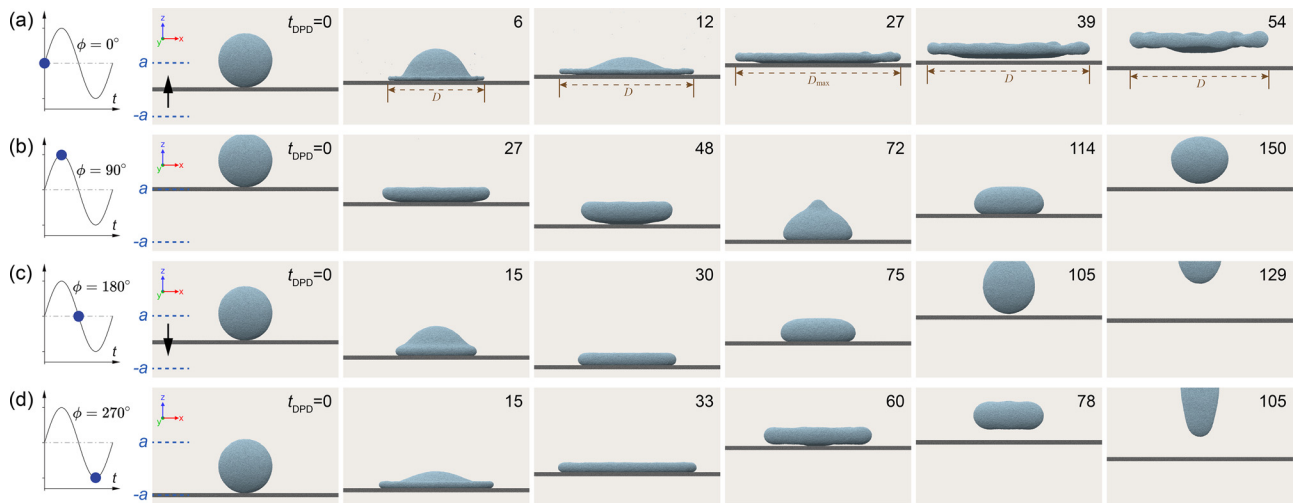
Figures 4(a) and 4(b) show the horizontal spreading diameter as a function of time. Figure 4(a) shows the cases as the solid substrate is moving upward when impact happens ( $\phi \in [-90^\circ, 90^\circ]$ ), and Fig. 4(b) shows the cases as the solid substrate is moving downward ( $\phi \in [90^\circ, 270^\circ]$ ). The results on a stationary substrate are plotted as a reference. Generally, the profiles have many similarities. For example, the time reaching the maximum diameter ( $D_{\max}$ ) is very close. However, the value of  $D_{\max}$  changes significantly and is highly dependent on  $\phi$ . As  $\phi$  moves from the highest position to the lowest position, the  $D_{\max}$  increases and then decreases. On the other hand, as  $\phi$  moves from the lowest position to the highest position, the  $D_{\max}$  decreases and then increases. We also notice some abnormal in the later stage, like in the cases of  $\phi = 90^\circ$  and  $\phi = 60^\circ$ . It is because the solid is moving upward, and the recoil of the droplet is suppressed.

Figure 4(c) summarizes  $D_{\max}$  in each case and plots them against the solid vertical position. The left end is the highest point ( $\phi = 90^\circ$ ), and the right end is the lowest point ( $\phi = 270^\circ$ ). All  $D_{\max}$  results are normalized by the initial droplet diameter ( $D_0$ ). The  $D_{\max}$  on non-vibrating substrate is plotted as reference. The green and purple colors indicate the solid is moving upward and downward when the impact happens, respectively.

We notice that the footprint of  $D_{\max}$  formed a closed loop. Generally, at the same impact height, the  $D_{\max}$  is always larger when the solid is moving upward than downward. The smallest  $D_{\max}$  is around  $\phi = 135^\circ$ , and the largest  $D_{\max}$  is around  $\phi = 0^\circ$ . The position with largest  $D_{\max}$  divergence is near the equilibrium position ( $\phi = 0^\circ$  and  $\phi = 180^\circ$ ). Overall, half of the data points are above the reference value, and half are below it.

Figures 5(a) and 5(b) show the vertical trajectories of the droplet ( $\text{COM}_z$ ) as a function of time. The  $\text{COM}_z$  is defined as the center of mass and is normalized by  $R_0$ . The time that impact happens is defined as  $T_{\text{DPD}} = 0$  for all cases. Figures 5(a) and 5(b) show the cases in which the solid is moving upward and downward when impact





**FIG. 3.** The snapshots of droplet impact on different phases of vibrating superhydrophobic substrate with  $We = 85.8$  and  $T_s = T_{c,ref}$ . (a)  $\phi = 0^\circ$ ; (b)  $\phi = 90^\circ$ ; (c)  $\phi = 180^\circ$ ; (d)  $\phi = 270^\circ$ . The droplets displayed the traditional spreading, recoil, and liftoff as impacting a traditional stationary solid surface, but show different contact time, area, and morphology.

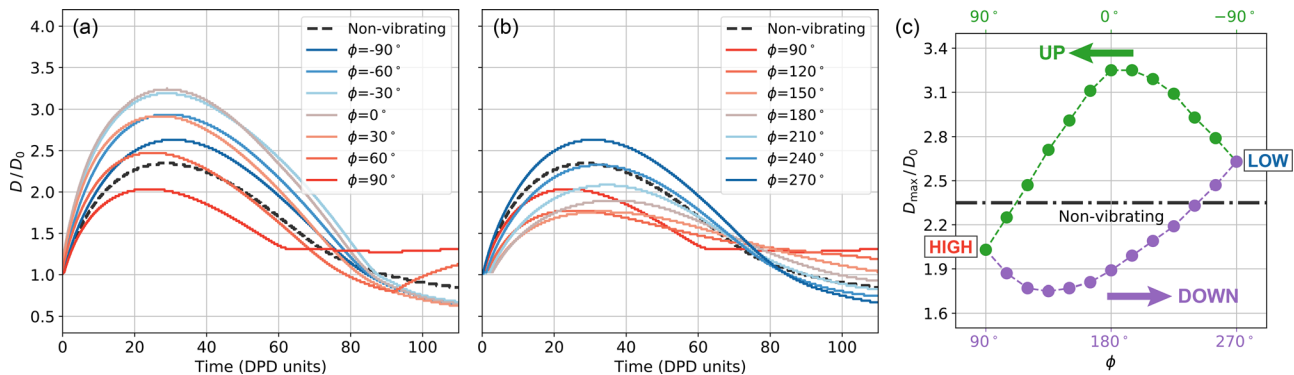


**FIG. 4.** The temporal evolution of droplet diameter for different impact phases, (a) from the lowest point ( $\phi = -90^\circ$ ) to the highest point ( $\phi = 90^\circ$ ) and (b) from the highest point ( $\phi = 90^\circ$ ) to the lowest point ( $\phi = 270^\circ$ ). (c) The maximum spreading diameter for different impact positions.

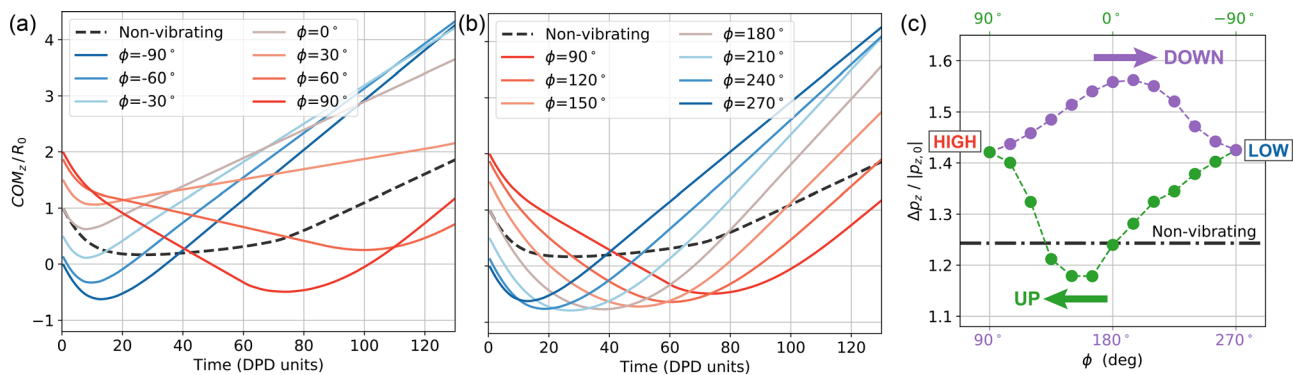


**FIG. 5.** The temporal evolution of vertical position of the droplet's center of mass for different impact phases, (a) from the lowest point ( $\phi = -90^\circ$ ) to the highest point ( $\phi = 90^\circ$ ) and (b) from the highest point ( $\phi = 90^\circ$ ) to the lowest point ( $\phi = 270^\circ$ ). (c) The momentum variation caused by the vibrating solid for different impact positions.

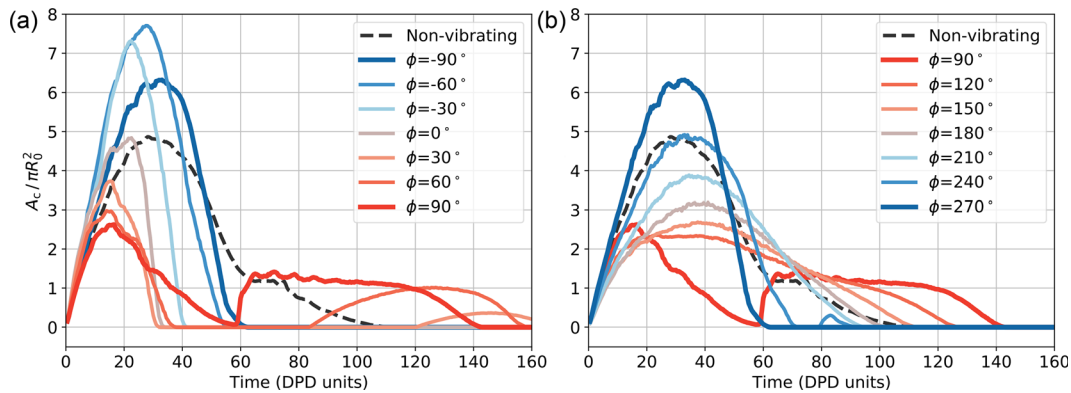


**FIG. 6.** The temporal evolution of the contact area for different impact phases, (a) from the lowest point ( $\phi = -90^\circ$ ) to the highest point ( $\phi = 90^\circ$ ) and (b) from the highest point ( $\phi = 90^\circ$ ) to the lowest point ( $\phi = 270^\circ$ ).

happens, respectively. The trajectory of  $\text{COM}_z$  on a non-vibrating surface is plotted as reference (dashed line). In the reference case,  $\text{COM}_z$  first descends at the speed of  $U_0$  and then keeps steady as the droplet is spreading horizontally. Then,  $\text{COM}_z$  starts to ascend because the droplet recoils and rebounds. The ascending speed keeps constant after the droplet detaches from the solid because there is no gravity in our DPD system.

In most Fig. 5(a) cases, the droplet velocity is reversed much faster than the reference. While in Fig. 5(b), velocity is reversed more gently. For the rebound speed (slope of the trajectory at the end), it is larger than the reference in most cases of both Figs. 5(a) and 5(b). We calculate the variation of momentum ( $\Delta p_z$ ) of each case based on the detach velocity and the impact velocity and plot them against the vertical position of impact in Fig. 5(c). The larger  $\Delta p_z$  implies a larger rebound speed, and  $\Delta p_z = 1.0$  implies a hypothetical scenario with zero rebound velocity. The results show that the maximum  $\Delta p_z$  happens at  $\phi = 195^\circ$ , and the minimum  $\Delta p_z$  happens at  $\phi = 30^\circ$ . Generally, most of the  $\Delta p_z$  is greater than the reference, indicating that the vibration overall promotes the droplet to rebound at a higher speed. Interestingly, the  $\Delta p_z$  or the

rebound speed at the highest and lowest position ( $\phi = 90^\circ$  and  $\phi = 270^\circ$ ) is almost the same.

Figure 6 shows the evolution of contact area ( $A_c$ ) with time for different  $\phi$ . Figures 6(a) and 6(b) summarize the results of  $\phi \in [-90^\circ, 90^\circ]$  and  $\phi \in [90^\circ, 270^\circ]$ , respectively. All  $A_c$  results are normalized by the droplet's projection area,  $\pi R_0^2$ . The results show that the maximum  $A_c$  is very sensitive to  $\phi$ , and the maximum in  $\phi = -60^\circ$  is nearly three times larger than that in  $\phi = 120^\circ$ . In addition to the peak value, the duration of the contact is also sensitive to  $\phi$ . Generally, the higher peak value is accompanied by a faster decay. We also notice some multiple contacts cases. For example,  $\phi = 60^\circ$  in Fig. 6(a), and  $A_c$  rises again at  $t_{\text{DPD}} = 85$  and decreases to zero at  $t_{\text{DPD}} = 155$ . The second contact can be far from the first contact, see  $\phi = -30^\circ$ , or very near to the first contact, even merged to the first contact, see  $\phi = 0^\circ$ .

Figures 7(a) and 7(b) illustrate a single contact case and a multiple contacts case, respectively. The droplet position is featured by the highest point (orange), the lowest point (green), and the center of mass (blue). The solid position is presented by the upper boundary of the solid (black). In Fig. 7(a), the impact phase is  $90^\circ$ . The droplet first

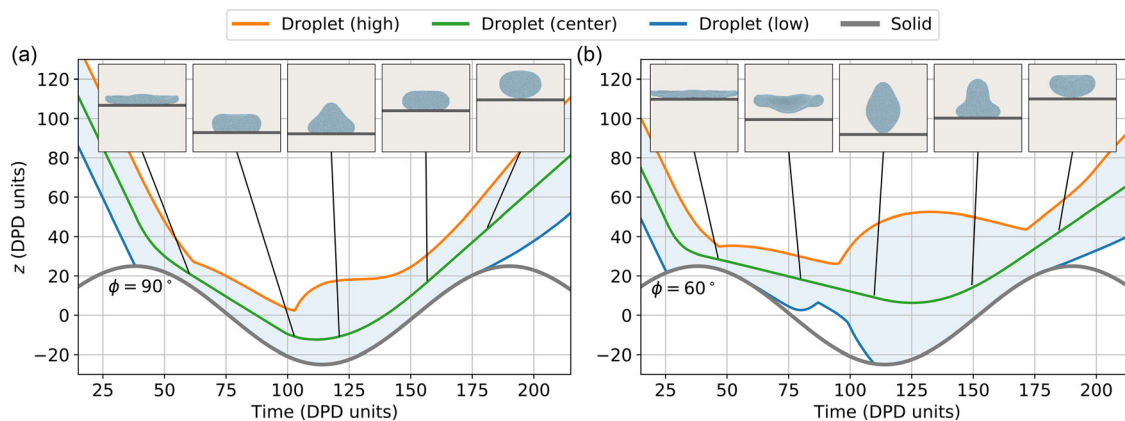


**FIG. 7.** The droplet position as a function of time (featured by the highest, lowest, and the center point). The vibrating solid is presented by the black line. The impact phase is a little different for (a) and (b); however, droplets experience single contact before final detach (a), while experience multiple contacts before final detach (b).

descends ( $< t_{\text{DD}} = 38$ ) at a constant speed and then impacts the solid with the lower boundary moves with the solid immediately. Meanwhile, the upper boundary moves at the initial speed for a long time if the impact does not happen and does not slow down until  $t_{\text{DD}} = 60$ . This phenomenon has also been observed and discussed in literature.<sup>47,58</sup> Then, the droplet spreads and recoils, while the droplet attaches to the solid all the time. Finally, the droplet detaches from the solid since the solid decelerates and moves downward.

In Fig. 7(b), the impact phase ( $\phi = 60^\circ$ ) is slightly ahead of Fig. 7(a). However, the whole contact is split into two, and the multiple contacts phenomenon appears. The difference starts from  $t_{\text{DD}} = 50$  when the droplet is fully spread. The velocity of the droplet's center is smaller than that in Fig. 7(a). As the solid keeps going down and the droplet starts to recoil, the droplet detaches from the solid. After that, the droplet turns into vertical elongated, and the contact happens again. As for the final detachment, it is similar to Fig. 7(a). We note that Figs. 7(a) and 7(b) only provide a simple comparison of the single and two contact phenomenon. With different combination of  $T_s$  and  $U_0$ , there may occur three or more contacts before the droplet finally rebound from the vibrating solid.

Due to the existence of multiple contacts phenomena, the measurement of  $T_c$  is more complicated than the traditional impact case. A common method is to use the time span from the first contact to the final detach as  $T_c$ . Using this method, Weisensee *et al.*<sup>26</sup> observed a critical impact phase at which the contact time transitions from a minimum to a maximum, leaving a discontinuity at the  $T_c(\phi)$  function. Here, we propose a new definition of  $T_c$ : the summation of each individual contact time. This definition is also physically meaningful and leads to different results.

Figure 8(a) shows the comparison of  $T_c$  by the two different definitions: span and summation. All  $T_c$  results are normalized by the reference contact time on non-vibrating surface ( $T_{c,\text{ref}}$ ). The resulting  $T_c$  is plotted as a function of impacting position. To start with, we check the duration of first contact, which is presented by hollow circles. For single contact cases, the first contact time equals the whole contact time. The most significant feature of the profile is the big gap at  $\phi = 90^\circ$ . Moreover, it is relatively smooth elsewhere. Then, we check the total contact time (span), which is presented by hollow diamonds. Like the first contact time, the

loop exhibits a huge gap but at a different impact phase,  $\phi = 0^\circ$ . Comparing the results with the first contact results, it is easy to identify the multiple contacts range ( $\phi \in (0^\circ, 90^\circ)$ ). This function reproduces the phenomenon that Weisensee *et al.*<sup>26</sup> presented in their paper, in which the contact time jumps from the minimum to the maximum at a critical phase. Finally, we check the results using our definition, presented by filled circles. In the multiple contacts range, the results fall between the first contact time and the total contact time (span). Take  $\phi = 30^\circ$  for example, comparing the three results, we conclude that the second contact only lasts for a short time, but happens much later after the first contact finishes. This makes that the presence of a quick and soft second contact dramatically increases the  $T_c$  by the time span definition and creates a discontinuity. On the other hand, the  $T_c$  by our definition seamlessly connects to the range of single contact and leaves no gap at both ends. By using our definition, the results formed a complete loop again.

The area-time integral characterizes the solid-liquid contact from another perspective other than contact time. Since its calculation is the integral of the contact area over time, it has no ambiguity regardless of single contact or multiple contacts. Figure 8(b) is the measured  $I$  as a function of  $\phi$ . The area-time integral results are continuous, like  $T_c$  by our definition. These results support the assumption that the effect of vibration on the solid-liquid contact may change continuously as  $\phi$  varies. Opposite to Fig. 8(a), which  $T_c$  is larger at  $\phi = 90^\circ$  than  $\phi = 270^\circ$ , the  $I$  at  $\phi = 90^\circ$  is smaller than  $\phi = 270^\circ$ . The  $\phi$  for maximum and minimum  $I$  ( $\phi = -60^\circ$  and  $\phi = 30^\circ$ ) are also quite different for that for  $T_c$  ( $\phi = 90^\circ$  and  $\phi = 0^\circ$ ). This deviation promotes us to design the vibration based on which aspect of contact is more of interest,  $T_c$  or  $I$ .

## B. The effect of vibrational frequency

The solid's vibrational frequency is another important factor affecting the dynamics of impacting droplets. In this section, we change  $f$  from 1/16 to 2 to check the droplet's response. The dynamics of droplet are evaluated from the aspects of  $D_{\text{max}}$ ,  $\Delta p$ ,  $T_c$ , and  $I$ . First, we illustrate that the probability of  $\phi$  is strongly influenced by  $\hat{f}$ , especially when  $\hat{f}$  is high. The probability analysis is necessary because it affects the average outcome when the droplet is randomly released or the impact phase is not controlled.

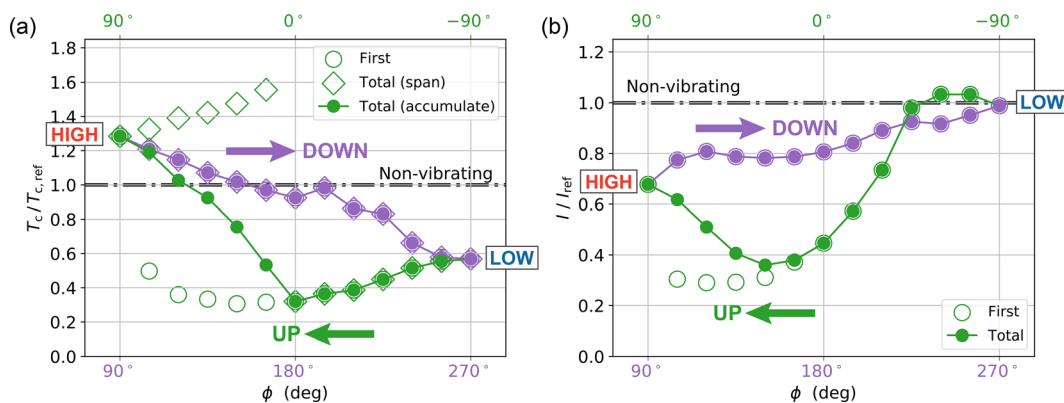


**FIG. 8.** (a) Contact time for different impact positions. For multiple contact cases, the first contact time, the total time as the span of all contacts, and the total time as the summation of each individual contact are compared. (b) Integral of contact area over time for different impact positions. The results show the area-time integral is continuous across different phases. The maximum and minimum values both occur when the solid is moving upward.



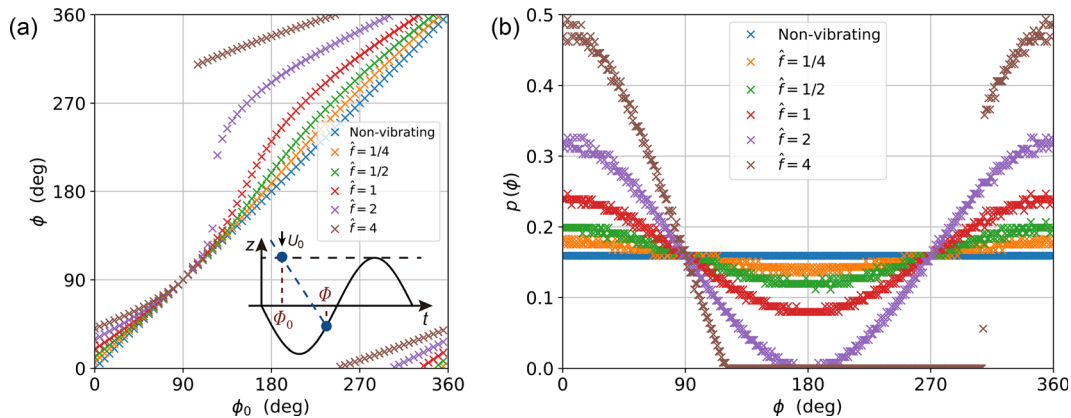


**FIG. 9.** The probability of different impact phases. (a) The impact phase as a function of the initial phase. The schematic inset shows the definition of initial and impact phases. (b) Probability density function for droplet impact at a certain phase. For  $\hat{f} = 1/4$ , impact becomes physically impossible for  $120^\circ < \phi < 307^\circ$ .

Figure 9 shows the probability of different  $\phi$  under different  $\hat{f}$ . We define  $\phi_0$  as the phase of the solid when the droplet's lowest part passes a marked height ( $z = a$ ), and  $\phi$  as the impact phase when the droplet first contacts the substrate. The inset of Fig. 9(a) illustrates the definition of the two variables. We run 3600 individual cases with uniformly distributed  $\phi_0$ , and Fig. 9(a) shows the resulting  $\phi$  as a function of  $\phi_0$ . For non-vibrating substrate, the results (blue cross) lie on the diagonal line, indicating that the probability of  $\phi$  equals the probability of  $\phi_0$ , which is uniform. If the substrate is vibrating slowly, for example,  $\hat{f} = 1/4$ , the  $\phi$  is slightly twisted from the diagonal line. As the vibrational period decrease, the results are influenced more obviously. For example, as  $\hat{f} = 2$ , no droplet can hit the substrate when  $\phi = 180^\circ$ .

Figure 9(b) is the probability of  $\phi$ ,  $p(\phi)$ , for different vibration frequencies. Generally, the probability profile deviates more from the reference horizontal line as  $\hat{f}$  gets higher. If the substrate's maximum speed is smaller than  $U_0$ , the probability profile is similar to a sinusoidal shape. Once the substrate's maximum speed exceeds  $U_0$ , the probability near  $\phi = 180^\circ$  drops to zero. Moreover,  $p(\phi)$  exhibits a discontinuity in the range of  $180^\circ$ – $360^\circ$ . This  $p(\phi)$  will be used to calculate the weighted averaged outcome for a specific substrate frequency.

Figure 10 summarizes the effect of vibrational frequency on  $D_{\max}$ ,  $\Delta p_z$ ,  $T_c$ , and  $I$ . Six different substrate frequencies are tested, i.e.,  $\hat{f} = 2, 1, 1/2, 1/4, 1/8$ , and  $1/16$ . The results are plotted against  $1/\hat{f}$ . For each frequency, 16 different  $\phi$  with  $\Delta\phi = 22.5^\circ$  are tested. The corresponding results on stationary substrates are plotted for comparison. These quantities are all normalized by the internal quantities of the dynamic system as in Sec. III A.

Figure 10(a) shows the influence of  $\hat{f}$  on  $D_{\max}$ . Each data point presents a simulation case. Considering some points are highly overlapped, we use color to present the data density. The dark and light colors indicate low and high density, respectively. One primary finding from Fig. 10(a) is that the larger  $1/\hat{f}$  generally leads to more converged results of different  $\phi$ . This is reasonable since extremely slowly moving substrate during contact is like stationary for the droplet. For  $1/\hat{f} = 0.5$  case, the data are more scattered. Note some data are marked with a cross at  $D_{\max}/D_0 = 4.0$ , this implies the droplet splashes in these cases. The  $D_{\max}$  is no longer applicable for the splashing

phenomenon. Overall, all data points seem to fall in an exponential envelope (dotted lines). It is helpful if we need to control the upper and lower limits of droplet spreading. The weighted averaged result (purple dashed line) for each  $\hat{f}$  is also plotted. The results show that the  $\hat{f}$  has less effect on the averaged  $D_{\max}$  rather than the distribution of  $D_{\max}$ .

Different from averaged  $D_{\max}$ , the averaged  $\Delta p_z$  is strongly affected by  $\hat{f}$  [Fig. 10(b)]. For  $1/\hat{f} = 0.5$ , the averaged momentum droplet get from the substrate is 40% more of that on a stationary substrate. All data points also exhibit some constraints of exponential boundaries (dotted lines).

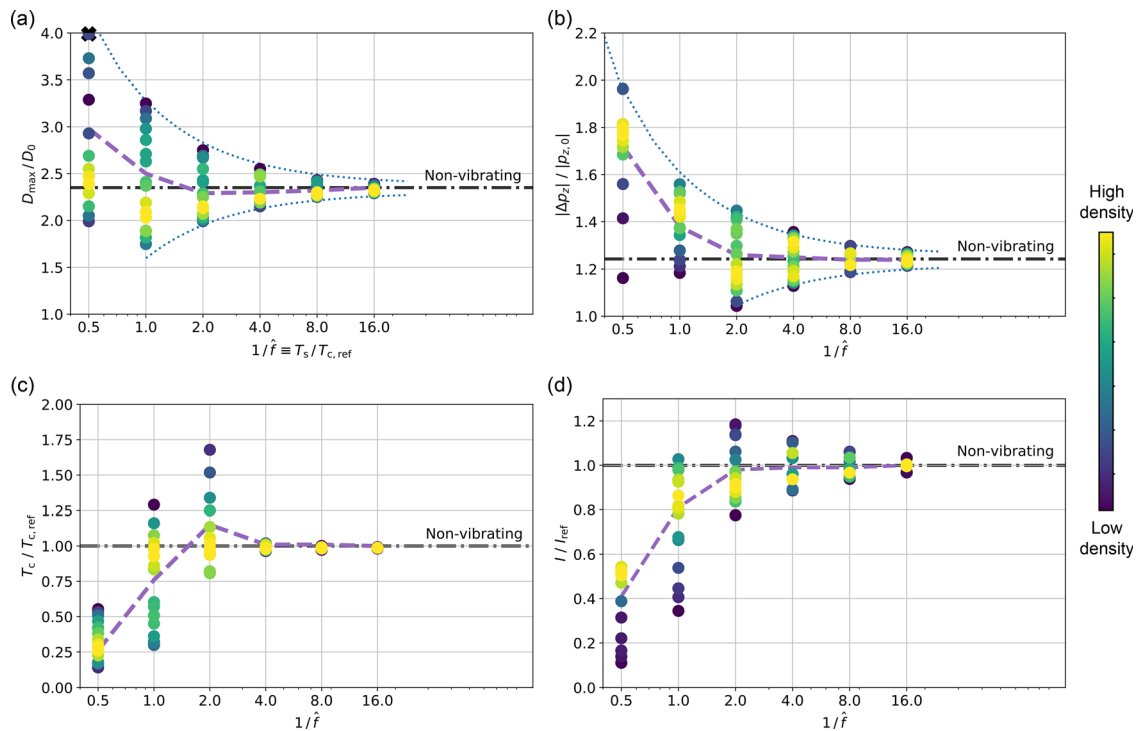
Figure 10(c) summarizes the  $T_c$  results. One finding is that for  $1/\hat{f} = 4.0$  and above, the results are highly converged to the reference  $T_c$ . It indicates that  $1/\hat{f} = 4.0$  is a threshold for manipulating  $T_c$  via vibrating solid. On the contrary,  $1/\hat{f} = 2.0$  leads to more scattered  $T_c$  data points, and the averaged result is slightly larger than the reference  $T_c$ . As  $1/\hat{f}$  decreases, the averaged  $T_c$  dramatically reduces. For  $1/\hat{f} = 0.5$ , the averaged result is only 30% of reference  $T_c$ . We note again that the  $T_c$  is measured as the summation of multiple individual contact time. These results are meaningful for applications in which reducing the contact time is of interest.

Figure 10(d) shows the results of  $I$ . Overall, the  $I$  is reduced by the vibrating substrate for every  $\hat{f}$  tested. The reduction effect is more obvious for higher vibrational frequencies. To obtain considerable reduction effect on  $I$ , setting  $1/\hat{f} \leq 1.0$  is necessary. For  $1/\hat{f} = 0.5$ , the weighted average  $I$  reaches 40% of  $I$  on stationary substrate.

#### IV. CONCLUSIONS

In this work, we use the MDPD method to investigate droplet impact on a vibrating superhydrophobic solid. The main findings are summarized as follows:

- On vibrating solids, the droplet may contact the substrate multiple times before finally rebounding away from the solid. We show that contact time's discontinuity at specific impact phase is associated with the definition of contact time for the multiple contacts scenario. Using the time span of all contacts, the definition will result in sudden change, while using the summation of



**FIG. 10.** The influence of vibrational frequency on the droplet dynamics. 16 simulations are conducted for each frequency. The result on stationary solid is shown for reference (dashdotted line). The averaged results for each frequency are calculated based on the probability of impact phase (dashed line). (a) The effect on the  $D_{\max}$ . (b) The effect on the momentum variation. (c) The effect on the contact time. (d) The effect on the area-time integral.

each individual contact time, the definition leads to continuous results. The contact time of the two definitions diverges only in multiple contacts scenario. This also explains why the discontinuity using the span definition was only observed with high vibrational frequencies.

- The integral of contact area over time can be considerably reduced at nearly all impact phases for dimensionless frequency  $\hat{f} = 1$ . The maximum reduction effect can reach over 60% when the impact phase is  $30^\circ$ . Moreover, the fact that the area-time integral changes continually with the impact phase supports the assumption that the effect of impact phase on the solid-liquid contact may be continuous.
- The probability of a droplet impacting certain  $\phi$  is affected by  $\hat{f}$ , especially when  $\hat{f}$  is small. The impact is even physically impossible for a specific range of  $\phi$ . This probability knowledge helps us to estimate the overall performance of vibrating substrate when the impact phase is not controlled.
- As  $\hat{f}$  decreases, generally, the distribution of  $D_{\max}$ ,  $\Delta p_z$ , and  $I$  for different phases is more converged, and the weighted averaged results get closer to the reference results on a stationary substrate.

Since many surfaces are not stationary and oscillating, this study can be useful to achieve controllable droplet impact outcomes. Considering our work is limited to the spread-recoil-rebound phenomenon, future work may extend the research to splashing, which involves higher vibrational frequencies.

## ACKNOWLEDGMENTS

The authors acknowledge the financial support from the National Natural Science Foundation of China (Nos. 12002242, 11902188, and 11872283), the Shanghai Science and Technology Talent Program (No. 19YF1417400), the Fundamental Research Funds for the Central Universities (No. 22120190207), and the National Key Research and Development Program of China (No. 2020YFB0311500).

## AUTHOR DECLARATIONS

### Conflict of Interest

The authors have no conflicts to disclose.

## DATA AVAILABILITY

The data that support the findings of this study are available from the corresponding author upon reasonable request.

## REFERENCES

- <sup>1</sup>T. Gilet and L. Bourouiba, "Fluid fragmentation shapes rain-induced foliar disease transmission," *J. Roy. Soc. Interface* **12**, 20141092 (2015).
- <sup>2</sup>A. K. Dickerson, P. G. Shankles, N. M. Madhavan, and D. L. Hu, "Mosquitoes survive raindrop collisions by virtue of their low mass," *Proc. Nat. Acad. Sci.* **109**, 9822–9827 (2012).
- <sup>3</sup>S.-S. Hsieh and S.-Y. Luo, "Droplet impact dynamics and transient heat transfer of a micro spray system for power electronics devices," *Int. J. Heat Mass Transfer* **92**, 190–205 (2016).

- <sup>4</sup>L. Mishchenko, B. Hatton, V. Bahadur, J. A. Taylor, T. Krupenkin, and J. Aizenberg, "Design of ice-free nanostructured surfaces based on repulsion of impacting water droplets," *ACS Nano* **4**, 7699–7707 (2010).
- <sup>5</sup>B. Amirzadeh, A. Louhghalam, M. Raessi, and M. Tootkaboni, "A computational framework for the analysis of rain-induced erosion in wind turbine blades, part II: Drop impact-induced stresses and blade coating fatigue life," *J. Wind Eng. Ind. Aerodyn.* **163**, 44–54 (2017).
- <sup>6</sup>Q. Zhang, M. He, J. Chen, J. Wang, Y. Song, and L. Jiang, "Anti-icing surfaces based on enhanced self-propelled jumping of condensed water microdroplets," *Chem. Commun.* **49**, 4516–4518 (2013).
- <sup>7</sup>Y. Cheng, S. Lu, W. Xu, H. Wen, and J. Wang, "Fabrication of superhydrophobic Au–Zn alloy surface on a zinc substrate for roll-down, self-cleaning and anti-corrosion properties," *J. Mater. Chem. A* **3**, 16774–16784 (2015).
- <sup>8</sup>J. Kim, "Spray cooling heat transfer: The state of the art," *Int. J. Heat Fluid Flow* **28**, 753–767 (2007).
- <sup>9</sup>D. B. van Dam and C. Le Clerc, "Experimental study of the impact of an ink-jet printed droplet on a solid substrate," *Phys. Fluids* **16**, 3403–3414 (2004).
- <sup>10</sup>H. Minemawari, T. Yamada, H. Matsui, J. Tsutsumi, S. Haas, R. Chiba, R. Kumai, and T. Hasegawa, "Inkjet printing of single-crystal films," *Nature* **475**, 364–367 (2011).
- <sup>11</sup>D. Attinger, C. Moore, A. Donaldson, A. Jafari, and H. A. Stone, "Fluid dynamics topics in bloodstain pattern analysis: comparative review and research opportunities," *Foren. Sci. Int.* **231**, 375–396 (2013).
- <sup>12</sup>C. Jossierand and S. T. Thoroddsen, "Drop impact on a solid surface," *Annu. Rev. Fluid Mech.* **48**, 365–391 (2016).
- <sup>13</sup>J. Eggers, M. A. Fontelos, C. Jossierand, and S. Zaleski, "Drop dynamics after impact on a solid wall: theory and simulations," *Phys. Fluids* **22**, 062101 (2010).
- <sup>14</sup>D. Richard, C. Clanet, and D. Quéré, "Contact time of a bouncing drop," *Nature* **417**, 811–811 (2002).
- <sup>15</sup>A. L. Yarin, "Drop impact dynamics: splashing, spreading, receding, bouncing...", *Annu. Rev. Fluid Mech.* **38**, 159–192 (2006).
- <sup>16</sup>X. Cheng, T.-P. Sun, and L. Gordillo, "Drop impact dynamics: Impact force and stress distributions," *Annu. Rev. Fluid Mech.* **54**, 57 (2022).
- <sup>17</sup>N. San Ha, Q. T. Truong, N. S. Goo, and H. C. Park, "Relationship between wingbeat frequency and resonant frequency of the wing in insects," *Bioinspiration Biomimetics* **8**, 046008 (2013).
- <sup>18</sup>K. Subrahmanyam and K. Kaza, "Vibration analysis of rotating turbomachinery blades by an improved finite difference method," *Int. J. Numer. Methods Eng.* **21**, 1871–1886 (1985).
- <sup>19</sup>D. Ding, D. Zhao, X. Zhang, X. Lan, C. Li, and B. Cui, "Investigation of vibration impacts on HVAC transformer from HVDC system under monopole operation," *IEEE Trans. Dielectrics Electr. Insul.* **23**, 1386–1392 (2016).
- <sup>20</sup>M. J. Griffin, "Discomfort from feeling vehicle vibration," *Veh. Syst. Dyn.* **45**, 679–698 (2007).
- <sup>21</sup>I. Oh, H. Cha, J. Chen, S. Chavan, H. Kong, N. Miljkovic, and Y. Hu, "Enhanced condensation on liquid-infused nanoporous surfaces by vibration-assisted droplet sweeping," *ACS Nano* **14**, 13367–13379 (2020).
- <sup>22</sup>J. Whitehill, A. Neild, T. W. Ng, S. Martyn, and J. Chong, "Droplet spreading using low frequency vibration," *Appl. Phys. Lett.* **98**, 133503 (2011).
- <sup>23</sup>W. Wang, C. Ji, F. Lin, J. Zou, and S. Dorbolo, "Water drops bouncing off vertically vibrating textured surfaces," *J. Fluid Mech.* **876**, 1041–1051 (2019).
- <sup>24</sup>J. B. Boreyko and C.-H. Chen, "Restoring superhydrophobicity of lotus leaves with vibration-induced dewetting," *Phys. Rev. Lett.* **103**, 174502 (2009).
- <sup>25</sup>W. Lei, Z.-H. Jia, J.-C. He, T.-M. Cai, and G. Wang, "Vibration-induced wenzel-cassie wetting transition on microstructured hydrophobic surfaces," *Appl. Phys. Lett.* **104**, 181601 (2014).
- <sup>26</sup>P. B. Weisensee, J. Ma, Y. H. Shin, J. Tian, Y. Chang, W. P. King, and N. Miljkovic, "Droplet impact on vibrating superhydrophobic surfaces," *Phys. Rev. Fluids* **2**, 103601 (2017).
- <sup>27</sup>M. Moradi, M. H. Rahimian, and S. F. Chini, "Numerical investigation of vibration-induced droplet shedding on smooth surfaces with large contact angles," *Phys. Rev. E* **100**, 023105 (2019).
- <sup>28</sup>H. J. Lee and H.-Y. Kim, "Control of drop rebound with solid target motion," *Phys. Fluids* **16**, 3715–3719 (2004).
- <sup>29</sup>H. Girard, D. Soto, and K. K. Varanasi, "Waterbowls: Reducing impacting droplet interactions by momentum redirection," *ACS Nano* **13**, 7729–7735 (2019).
- <sup>30</sup>D. Wang, D. Tan, and N. Phan-Thien, "A lattice boltzmann method for simulating viscoelastic drops," *Phys. Fluids* **31**, 073101 (2019).
- <sup>31</sup>C. Lin, K. Zhang, X. Chen, L. Xiao, S. Chen, J. Zhu, and T. Zou, "Reducing droplet contact time and area by craterlike surface structure," *Phys. Rev. Fluid* **6**, 83602 (2021).
- <sup>32</sup>M. Arienti, W. Pan, X. Li, and G. E. Karniadakis, "Many-body dissipative particle dynamics simulation of liquid/vapor and liquid/solid interactions," *J. Chem. Phys.* **134**, 204114 (2011).
- <sup>33</sup>X. Bian, Z. Li, and N. Adams, "A note on hydrodynamics from dissipative particle dynamics," *Appl. Math. Mech.* **39**, 63–82 (2018).
- <sup>34</sup>L. Lu, Z. Li, H. Li, X. Li, P. G. Vekilov, and G. E. Karniadakis, "Quantitative prediction of erythrocyte sickling for the development of advanced sickle cell therapies," *Sci. Adv.* **5**, eaax3905 (2019).
- <sup>35</sup>L. Xiao, C. Lin, S. Chen, Y. Liu, B. Fu, and W. Yan, "Effects of red blood cell aggregation on the blood flow in a symmetrical stenosed microvessel," *Biomech. Model. Mechanobiol.* **19**, 159–171 (2020).
- <sup>36</sup>X. Qi, S. Wang, S. Ma, K. Han, X. Bian, and X. Li, "Quantitative prediction of rolling dynamics of leukocyte-inspired microroller in blood flow," *Phys. Fluids* **33**, 121908 (2021).
- <sup>37</sup>Y. Deng, H.-y. Chang, and H. Li, "Recent advances in computational modeling of biomechanics and biorheology of red blood cells in diabetes," *Biomimetics* **7**, 15 (2022).
- <sup>38</sup>C. Lin, S. Chen, L. Xiao, and Y. Liu, "Tuning drop motion by chemical chessboard-patterned surfaces: a many-body dissipative particle dynamics study," *Langmuir* **34**, 2708–2715 (2018).
- <sup>39</sup>K. Zhang, Z. Li, and S. Chen, "Analytical prediction of electrowetting-induced jumping motion for droplets on hydrophobic substrates," *Phys. Fluids* **31**, 081703 (2019).
- <sup>40</sup>Z. Li, G. Hu, Z. Wang, Y. Ma, and Z. Zhou, "Three dimensional flow structures in a moving droplet on substrate: A dissipative particle dynamics study," *Phys. Fluids* **25**, 072103 (2013).
- <sup>41</sup>D. Pan, G. Zhao, Y. Lin, and X. Shao, "Mesoscopic modelling of microbubble in liquid with finite density ratio of gas to liquid," *EPL (Europhys. Lett.)* **122**, 20003 (2018).
- <sup>42</sup>C. Lin, Z. Li, L. Lu, S. Cai, M. Maxey, and G. E. Karniadakis, "Operator learning for predicting multiscale bubble growth dynamics," *J. Chem. Phys.* **154**, 104118 (2021).
- <sup>43</sup>C. Lin, L. Yang, F. Chen, S. Chen, and H. Yin, "A dissipative particle dynamics and discrete element method coupled model for particle interactions in sedimentation toward the fabrication of a functionally graded material," *Colloids Surf. A Physicochem. Eng. Asp.* **604**, 125326 (2020).
- <sup>44</sup>S. Chen, N. Phan-Thien, X. Fan, and B. C. Khoo, "Dissipative particle dynamics simulation of polymer drops in a periodic shear flow," *J. Non-Newtonian Fluid Mech.* **118**, 65–81 (2004).
- <sup>45</sup>X. Li, Y. Tang, H. Liang, and G. E. Karniadakis, "Large-scale dissipative particle dynamics simulations of self-assembled amphiphilic systems," *Chem. Comm.* **50**, 8306–8308 (2014).
- <sup>46</sup>C. Lin, M. Maxey, Z. Li, and G. E. Karniadakis, "A seamless multiscale operator neural network for inferring bubble dynamics," *J. Fluid Mech.* **929**, A18 (2021).
- <sup>47</sup>C. Lin, D. Cao, D. Zhao, P. Wei, S. Chen, and Y. Liu, "Dynamics of droplet impact on a ring surface," *Phys. Fluids* **34**, 012004 (2022).
- <sup>48</sup>B. R. Mitchell, J. C. Klewicki, Y. P. Korkolis, and B. L. Kinsey, "The transient force profile of low-speed droplet impact: measurements and model," *J. Fluid Mech.* **867**, 300–322 (2019).
- <sup>49</sup>Y. Wang, Y. Wang, and S. Wang, "Droplet impact on cylindrical surfaces: Effects of surface wettability, initial impact velocity, and cylinder size," *J. Colloid Interface Sci.* **578**, 207–217 (2020).
- <sup>50</sup>C. Wang, X. Wu, H. Zhang, P. Hao, F. He, and X. Zhang, "A many-body dissipative particle dynamics study of eccentric droplets impacting inclined fiber," *Phys. Fluids* **33**, 042001 (2021).
- <sup>51</sup>X. Li, H. Li, D. Zheng, and Y. Wang, "Many-body dissipative particle dynamics study of droplet impact on superhydrophobic spheres with different size," *Colloids Surf. A* **618**, 126493 (2021).
- <sup>52</sup>P. Español and P. Warren, "Statistical mechanics of dissipative particle dynamics," *Europhys. Lett.* **30**, 191 (1995).

- <sup>53</sup>P. B. Warren, “Vapor-liquid coexistence in many-body dissipative particle dynamics,” *Phys. Rev. E* **68**, 066702 (2003).
- <sup>54</sup>H. Kim, U. Park, C. Lee, H. Kim, M. Hwan Kim, and J. Kim, “Drop splashing on a rough surface: How surface morphology affects splashing threshold,” *Appl. Phys. Lett.* **104**, 161608 (2014).
- <sup>55</sup>Z. Li, X. Bian, Y. Tang, and G. E. Karniadakis, “A dissipative particle dynamics method for arbitrarily complex geometries,” *J. Comput. Phys.* **355**, 534–547 (2018).
- <sup>56</sup>C. Zhang, Z. Wu, C. Shen, Y. Zheng, L. Yang, Y. Liu, and L. Ren, “Effects of eigen and actual frequencies of soft elastic surfaces on droplet rebound from stationary flexible feather vanes,” *Soft Matter* **16**, 5020–5031 (2020).
- <sup>57</sup>C. Clanet, C. Béguin, D. Richard, and D. Quéré, “Maximal deformation of an impacting drop,” *J. Fluid Mech.* **517**, 199–208 (2004).
- <sup>58</sup>L. Gordillo, T.-P. Sun, and X. Cheng, “Dynamics of drop impact on solid surfaces: evolution of impact force and self-similar spreading,” *J. Fluid Mech.* **840**, 190–214 (2018).